

Improved Resolution Backscatter Measurements with the *SeaWinds* Pencil-Beam Scatterometer

Michael W. Spencer and Chialin Wu

Jet Propulsion Laboratory, California Institute of Technology
MS 300-319, 4800 Oak Grove Dr., Pasadena, CA 91109-8099
mws@shiohaze.jpl.nasa.gov (818) 354-1175

David G. Long

Brigham Young University
Dept. of Electrical and Computer Engineering, 459 CB
Provo, UT 84602
long@ee.byu.edu (801) 378-4383

September, 1998

Abstract

The *SeaWinds* scatterometer will fly on the NASA *Quikscat* spacecraft in 1998, and on the Japanese ADEOS-II mission in 2000. In addition to providing ocean surface wind estimates for use by weather forecasters, these flights will generate a global Ku-Band backscatter data set for a variety of climate studies. *SeaWinds* employs a compact “pencil-beam” design rather than the “fan-beam” approach previously used with NSCAT on ADEOS-I and the AMI scatterometer on ERS-1,2. As originally envisioned and reported, the resolution of the *SeaWinds* backscatter measurements were to be antenna beam-width limited. In order to satisfy an emerging demand for higher resolution backscatter data, however, the *SeaWinds* signal processing design has been significantly modified. Here, the various options considered for improving the resolution of the *SeaWinds* measurements are discussed, and the selected hardware modification – the addition of digital range filtering – is described. The radar equation specific to a rotating pencil-beam scatterometer with range filtering is developed, and the challenges associated with calibrating the resulting improved resolution measurements are discussed. A formulation for assessing the variance of the measurements due to fading and thermal noise is presented. Finally, the utility of improved resolution *SeaWinds* measurements for land and ice studies is demonstrated by simulated imaging of a synthetic Earth backscatter scene.

I. Introduction and Background

Spaceborne wind scatterometry has become an increasingly important tool in the effort to monitor the Earth's climate, forecast weather, and study ocean/atmosphere interaction. To continue and expand upon the foundation provided by the recent flight of the NASA Scatterometer (NSCAT), NASA has developed the *SeaWinds* instrument which is scheduled for two flights: first on the dedicated *Quikscat* mission in November 1998, and then as a facility instrument aboard the second Japanese Advanced Earth Observation Satellite (ADEOS-II) in 2000.

A. *SeaWinds* Scatterometer Design

As with all scatterometers, *SeaWinds* will obtain an estimate of the wind vector by measuring ocean surface radar backscatter cross section (σ^o) at multiple azimuth angles. The geophysical model function, which relates wind speed and direction to backscatter cross section, is then numerically inverted to infer the near surface wind. In a significant design departure from previously flown “fan-beam” scatterometer systems, however, *SeaWinds* is a “pencil-beam” design.

With fan-beam scatterometers, such as NSCAT and the AMI scatterometer on the European Earth Remote Sensing satellite series (ERS-1 and 2), several fixed antennas are deployed to cast long, narrow illumination patterns at the multiple incidence angles required for wind retrieval [1] [12]. The narrow dimension of the antenna beam pattern provides resolution in the along-track direction, and Doppler or range filtering is employed to provide cross-track resolution. The antenna structures are typically about three meters in length and require large unobstructed fields-of-view on the spacecraft.

By contrast, planned pencil-beam systems employ a single, approximately one meter parabolic dish which is conically scanned about the nadir axis to provide multiple azimuth measurements [13] [17] (see Fig.'s 1 and 2). A key advantage to pencil-beam systems is that, because of their more compact design, they are much easier to accommodate on spacecraft without the necessity of complex deployment schemes or severe field-of-view constraints. In an era where smaller space missions with faster development times are often mandated – as is the case with the *Quikscat* mission, for example [4] – such a reduction in payload

size is highly desirable. An additional advantage to pencil-beam systems is that because they measure ocean backscatter at a constant incidence angle suitable for wind retrieval, there is no “nadir gap” in swath coverage as there is for fan-beam systems. The resulting contiguous swath offers a significant improvement in Earth coverage. For these reasons, the pencil-beam design has been adopted for *SeaWinds* and planned follow-on systems into the next century [14].

B. Utility of Higher Resolution Measurements with *SeaWinds*

The original design of the *SeaWinds* instrument, which was developed previous to the flight of NSCAT, is described in [13]. As originally planned, the spatial resolution of the σ^0 measurements collected with *SeaWinds* were to be “beam-limited” – i.e., the dimensions of the σ^0 cell are determined by the antenna beam footprint on the surface. For the *SeaWinds* one meter antenna, the resulting footprint dimensions are roughly 25 km by 35 km (see Table 1). This resolution approach was selected for two reasons: 1) it satisfied resolution requirements for the primary scatterometer mission to measure synoptic-scale global winds, and 2) it enabled high radiometric precision and calibration accuracy to be achieved with a very simple hardware design.

The success of the NSCAT mission, however, demonstrated the benefits of measuring surface backscatter at higher resolution. Although NSCAT was also designed primarily as a synoptic wind instrument, the inherent spatial resolution of the backscatter measurements is somewhat higher than that originally planned for *SeaWinds*. The narrow NSCAT antenna patterns were Doppler filtered to form σ^0 “cells” of approximately 8 km by 25 km. These measurements proved to be extremely useful in new scientific applications for spaceborne scatterometry. Wind fields constructed by utilizing the full resolution capability of NSCAT exhibit mesoscale motions in detail [3],[6], allowing the potential for more in depth analysis of storms, frontal zones, orographic effects, and coastal phenomena.

In addition to ocean wind vector retrieval, scatterometer σ^0 measurements are also finding increased applicability in land and ice studies, as surface backscatter is a sensitive indicator of environmental change. The utility of the scatterometer data for land and ice studies is significantly expanded by using a technique referred to as enhanced resolution imaging (ERI). With ERI, multiple passes of overlapping scatterometer data over the same

region are combined to solve for backscatter images that have higher resolution than the original measurements [7]. Essentially, this process is equivalent to a deconvolution of the σ° measurement spatial response function. Although images obtained by ERI are still of much lower resolution than that obtainable with SAR's, they have the advantage of very frequent global coverage. Images obtained by ERI have been used in studies of polar ice and the Amazon rain forest [8] [11].

Examples of algorithms that have been successfully employed to achieve resolution enhancement of microwave remote sensing data include Backus-Gilbert Inversion (BGI) and Scatterometer Image Reconstruction with Filtering (SIRF) [10]. As observed with the SIRF algorithm, the practical resolution achievable with ERI is roughly equivalent to the *narrowest* dimension of the σ° measurement cell. For NSCAT, this limiting resolution is approximately 8 km. If beam-limited *SeaWinds* σ° cells are used, however, the corresponding enhanced resolution achievable is only about 25 km.

Thus, in order to extend the valuable higher resolution capability demonstrated with NSCAT to the next series of Ku-band scatterometers, the *SeaWinds* design must be modified to produce backscatter measurements with improved resolution. A challenge accompanying any such modification is that high radiometric precision and calibration accuracy – characteristics which allow the scatterometer to retrieve winds and detect global change – must be preserved.

This paper discusses the various options and trade-offs considered for improving the resolution of a scanning pencil-beam scatterometer. The specific design modification implemented on *SeaWinds* for flights on *Quikscat* and ADEOS-II – the addition of range discrimination capability – is described. In Section III, the new challenges associated with calibrating these higher resolution σ° 's are addressed, and the radar equation for a rotating pencil-beam scatterometer with range filtering is presented. Also in Section III, the issue of measurement precision is addressed and a formulation for the measurement variance for the higher resolution σ° 's is given. Finally, in Section IV, simulation results are shown which demonstrate the enhanced backscatter imaging capability achievable with the modified system relative to what was originally achievable with the beam limited system. Although the presentation here is primarily directed towards describing the *SeaWinds* system, the principles developed are applicable to future scanning pencil-beam scatterometer designs as

well.

II. Improved Resolution Approach

A. Range vs. Doppler Discrimination

Before describing the specific range discrimination modification implemented on *SeaWinds*, it is insightful to discuss the reasons for selecting this approach over other resolution improvement options. The overriding consideration was that because the modifications were to be made late in the hardware development, only a minimum of changes to the overall instrument architecture could be accommodated. Further, the ability to achieve high radio-metric accuracy and adequate Earth coverage could not be compromised. In general these constraints implied only changes to the radar modulation and signal processing electronics, with no changes to the spacecraft orbit, antenna subsystem, or transmitter, and with only a modest increase in data rate.

With these limitations in mind, it is next instructive to consider the overall geometry and range/Doppler characteristics of the *SeaWinds* backscatter measurement. As described in [13], *SeaWinds* employs a one meter diameter dish antenna with offset feeds to generate two pencil-beams – the “inner” beam at an off-nadir angle of 40° and the “outer” beam at an off-nadir angle of 46° (see Fig. 1). The antenna is then conically scanned such that each point on the Earth within the inner 700 km of the swath is view from four different azimuth directions – twice by the inner beam looking forward then aft, and twice by the outer beam in a similar fashion. Other relevant parameters for the antenna and scan geometry are given in Table 1.

The approximate dimensions of the antenna two-way 3 dB footprint contour, along with the associated two-way iso-range and iso-Doppler lines are conceptually illustrated in Fig. 3. Two representative cases are shown: the case where the beam is scanned to an azimuth angle of 0° (beam looking in the direction of spacecraft motion), and the case where the beam is scanned to an azimuth of 90° (beam looking perpendicular to spacecraft motion). Note that for the 0° azimuth case, the iso-range and iso-Doppler lines are approximately parallel, whereas in the 90° case they are nearly perpendicular. Other azimuth angles will yield various intermediate states of these two cases, with the range and Doppler lines

slanting with respect to each other.

Ideally, we desire a processing scheme which resolves the footprint in two orthogonal dimensions simultaneously – in effect obtaining a low resolution SAR measurement with both range and Doppler resolution. Unfortunately, this goal can not be achieved with the existing *SeaWinds* architecture. The primary reason for this is that the diameter of the *SeaWinds* antenna (one meter) is smaller than that required to simultaneously avoid both range and Doppler ambiguities [16]. To see this, consider that the beam fill time – the difference in round trip flight time from the near edge to the far edge of the antenna footprint – is approximately 0.28 ms. To avoid range ambiguities within the footprint, this implies a *maximum* PRF of 3.6 kHz. The total Doppler bandwidth across the footprint, however, is approximately 10 kHz and thus requires a *minimum* 10 kHz PRF in order to unambiguously resolve the scene in azimuth. A measurement without ambiguity difficulties would require an antenna diameter in excess of two meters to achieve a sufficiently narrow beamwidth, violating a key requirement that the instrument be physically compact. Even if the antenna was large enough, as the antenna is scanned near 0° or 180° azimuth the Doppler and range lines are nearly parallel, making resolution in two dimensions difficult.

As an alternative, we consider performing either pure range filtering or pure Doppler filtering to achieve spatial “slices” through the antenna footprint, where resolution is only improved in one dimension. Again referring to Fig. 3, we have illustrated idealized slices (or “cells,” as they are also called) formed by range discrimination or Doppler discrimination with dark and light shaded regions respectively. As will be demonstrated more fully in Section IV, the fact that we can improve resolution in at least one dimension is still of significant benefit, particularly for land and ice images constructed with ERI. To decide whether range or Doppler filtering should be employed for *SeaWinds*, two issues were considered: backscatter measurement variance and the geometrical orientation of the resultant σ° cells.

The measurement variance issue is discussed in more detail in Section III, but a brief argument is given here to justify the filtering strategy selected for *SeaWinds*. Scatterometer measurements of surface σ° are noisy due to Rayleigh fading and because of the presence of thermal noise. A key goal of scatterometer design is to minimize the σ° noise variance. When the signal-to-noise ration (SNR) is large – as it generally is for land, ice, and moderate

to high ocean winds – Rayleigh fading is the dominant factor, and the variance of each σ° measurement is related to the number of independent “looks” achieved [16].

In the Doppler filtering case, the maximum number of “looks” available is related to the Doppler frequency resolution associated with the transmit signal. For the selected *Sea Winds* timing, the maximum integration time on each scene is 1.5 ms, implying a best Doppler resolution of 666 Hz. Given that the Doppler bandwidth of the illuminated region is about 10 kHz, approximately 15 independent looks are available across the entire footprint. If the footprint is equally divided into four slices, this is equivalent to four looks per slice, corresponding to a measurement standard deviation of 50%. Measurement variance can not be further improved without lengthening the transmit pulse, which is not allowed by the timing constraints.

In the range filtering case, however, the inherent resolution is a function of the bandwidth of the modulated transmit pulse. If the transmit pulse is modulated with a linear chirp at a rate of 250 kHz/ms, the resulting pulse will have a bandwidth of 375 kHz, corresponding to a range resolution of about 0.8 km. Again, if the footprint is divided equally into four slices, this implies 12.5 looks per slice, or a measurement standard deviation of 28%. If SNR is sufficiently high, the measurement variance can be further improved in the range filtering case by increasing the bandwidth of the transmitted pulse. The flexibility to improve the measurement accuracy of the slices, and consequently the accuracy of geophysical products such as winds and surface images, by adjusting the transmit modulation bandwidth is a key advantage of the range filtering approach.

A secondary consideration is the orientation of the σ° slices. Because ERI algorithms utilize many overlapping σ° measurements, possibly from multiple orbits, it is generally desirable to have the slices oriented at different angles so that resolution may be enhanced effectively in all directions. As shown in Fig. 3, this requirement favors range filtering because the orientation of the cells rotate with azimuth angle, as opposed to Doppler filtering where the cells are oriented roughly perpendicular with the direction of flight. Because of the above described advantages in measurement variance and cell orientation, the range discrimination approach was chosen to form the *Sea Winds* improved resolution cells.

B. Range Filtering Implementation

Because of the relatively low peak power available with the *SeaWinds* transmitter, a CCF technique was selected to achieve range resolution. This type of processing is similar to that employed by other spaceborne radar instruments (e.g. [18]), and minimizes modifications to the existing “low resolution” *SeaWinds* design. A functional diagram of the *SeaWinds* radar is shown in Fig. 4. Upon command from the timing controller, the transmitter, which consists of a modulated signal generator driving a traveling wave tube (TWT) amplifier, issues a 1.5 ms duration, 110 Watt Ku-Band pulse. In the previous design, the pulse was MSK modulated to optimize the measurement variance for the simple “non-matched” square law detection scheme used to obtain beam-limited σ^0 cells [9] [13]. For range discrimination, the transmit pulse is now modulated with a linear frequency chirp at a chirp rate of 250 kHz/ms for a total bandwidth of 375 kHz. A discussion of how this specific chirp rate was selected is in Section III, Subsection B.

Due to the motion of the satellite relative to the Earth, a gross Doppler shift of between +/- 500 kHz is imparted to the echo return, depending on the antenna azimuth position. In the *SeaWinds* design, this Doppler shift is pre-compensated by tuning the transmit carrier frequency to 13.402 GHz minus the expected Doppler shift from the footprint center location. Pre-compensating for Doppler shift produces an echo signal that always occurs at the same baseband frequency after downconversion. The transmit pulse is routed to either the inner or outer beam through a coaxial rotary joint to the spinning section of the antenna assembly. An important feature of any scatterometer is the accurate calibration of the transmit power and receiver gain (see Section III, Subsection A). These parameters are measured simultaneously by periodically injecting the transmit pulse, attenuated by a known amount, into the receiver via the calibration loop coupler.

The pulse repetition and echo gate timing, which is designed to provide a sufficiently dense sampling of σ^0 measurements on the surface as the antenna rotates, is shown in Fig. 5. Transmit pulses occur every 5.4 ms and alternate between the inner and outer beams. This produces an effective PRF of 92.5 kHz for each beam. The round trip flight times for the inner and outer beam pulses is approximately 7.3 ms and 8.3 ms respectively, and thus each echo returns after the succeeding transmit pulse. In Fig. 5, the echo returns

are depicted as trapezoids to indicate dispersion due to the antenna footprint fill time of approximately 0.3 ms.

The echo signal processing, which constitutes the most significant modification made to implement range discrimination, is diagramed in Fig. 6. After downconversion to baseband, the echo is digitally sampled. The total echo return, which is the sum of all the echo returns from scatterers across the illuminated region, is then digitally “deramped” by mixing with a chirped reference signal. This operation effectively converts range delays into frequency shifts – i.e., each discrete frequency in the deramped signal corresponds to the return from a given range line on the surface (plus a small Doppler shift effect discussed in Section III). To extract the range information, a DFT (implemented as an FFT) is performed on the deramped signal and a periodogram is formed by applying a magnitude square operation. The periodogram bins are then summed into twelve range slice energy measurements to be telemetered to the ground.

To illustrate further Fig. 7 shows a conceptual plot of the deramped power spectral density (shaded region) and slice bandwidths. For the selected *Sea Winds* chirp rate of 250 kHz/ms, the deramped spectral density has a 3 dB bandwidth (B_{3dB}) of approximately 40 kHz. The returned energy for the j th slice, C_{sn}^j , is formed by summing adjacent periodogram bins over the slice bandwidth B_s . For *Sea Winds* it was decided to construct σ° cells which resolve the surface to approximately 7 km in the narrow (range) direction. For the given chirp rate, this corresponds to $B_s = 8.3$ kHz. This bandwidth is used for the ten innermost slices. The two outermost slices are termed “guard slices” and are assigned a somewhat larger bandwidth. The total bandwidth spanned by all twelve slices, B_e , is approximately 200 kHz, and is designed so as to capture the entire deramped echo spectrum.

As in the previous design [13], a wide-band “noise-only” measurement (C_{no}) is made by passing the return echo and system noise through a filter of bandwidth $B_n = 1$ MHz, square-law detecting, and then integrating. This measurement is used in determining the thermal noise background component to C_{sn}^j which must be subtracted off before σ° can be estimated.

C. σ° Estimation

The estimation of σ° from the telemetered measurements is essentially a two step process. First, an estimate of the thermal noise contribution (instrument plus Earth scene) to a given slice measurement, P_n^j , must be subtracted from the slice measurement, C_{sn}^j , to yield an estimate of the “signal-only” power, P_s^j ,

$$P_s^j = C_{sn}^j - P_n^j. \quad (1)$$

For low wind speeds, the noise contribution may be ten times the signal strength, and thus the accurate determination of P_n^j is a crucial step (see Appendix A).

The second step is to relate the signal-only echo energy to a value of σ° on the Earth’s surface by applying the radar calibration parameter, X ,

$$\sigma^\circ = \frac{P_s^j}{X}. \quad (2)$$

Eq. (2) is a shorthand expression for the distributed target radar equation [16]. Here, X incorporates all instrumental and geometrical parameters (antenna gain, transmit power, slant range, etc.) necessary to define the relationship between detected echo energy and σ° . The radar equation specific to a scanning pencil-beam scatterometer with digital range filtering is developed in the next section.

III. Backscatter Measurement Accuracy

In the previous section, the overall resolution approach, along with the selected signal processing implementation, was described. Although it is clear that resolution is easily enhanced by the addition of range filtering, it is critical that the issue of σ° measurement accuracy be addressed as well. A fundamental requirement of scatterometer instruments is the ability to measure surface backscatter with very high accuracy. Such accuracy is required to retrieve winds and detect long-term climatic change. In general, achieving the desired measurement accuracy is more difficult with σ° cells formed by “range slicing” than in the simple beam-limited case, and requires the introduction of new formulations for the radar equation and backscatter measurement variance calculation. This section provides the necessary analytical framework for addressing the issue of σ° accuracy for *ScaWinds*

with digital range filtering, and discusses several of the trade-offs that must be conducted to optimize performance. We address two main aspects of measurement accuracy: a) σ° calibration associated with the X parameter in Eq. (2), and b) σ° measurement variance associated with random fluctuations in P_s^j due to fading and thermal noise.

A. σ° Calibration

Calibration accuracy refers to the scatterometer's ability to determine the true backscatter cross section given the intensity of the echo return. In essence, it is the accuracy with which we know the radar parameter X in Eq. (2). In general, calibration error can be divided into two sources: radiometric errors, which are caused by uncertainty in our knowledge of instrument component gains and losses, and geometric errors, which arise chiefly from imperfect knowledge of the exact pointing of the antenna pattern. As will be discussed, it is primarily geometric errors which limit the calibration performance of a well designed scatterometer instrument.

It is also important to differentiate between *absolute* and *relative* calibration errors. An absolute error is the degree to which a measurement of σ° differs from the "true" value. A relative calibration error, however, is the difference in absolute error between two σ° measurements separated in space and/or time. Because we are most interested in detecting either spatial or temporal *change* in surface backscatter, it is particularly important to minimize relative error. To produce marine wind fields with the desired accuracy and to allow maximum sensitivity to climatologically induced changes in surface backscatter, relative calibration accuracy on the order of 0.1 dB is desired. This challenging goal requires a detailed consideration of all radiometric and geometric factors effecting the X parameter for each σ° cell.

Expression for X

The first step in the calibration of the instrument involves the development of an expression for the parameter X . In deriving X , we track the radar signal through its interaction with the surface and the subsequent echo signal processing.

The transmitted signal can be written as

$$T(t) = \sqrt{E_t} p(t) e^{j2\pi[f_c + f_{dc} + \frac{1}{2}\mu t]t} \quad (3)$$

where t is time from transmit pulse onset, E_t is total energy in transmit pulse, $p(t)$ is the transmit pulse power envelope such that $\int p^2(t) = 1$, f_c is the transmit carrier frequency, f_{dc} is the Doppler offset frequency, and μ is the chirp rate.

The echo return from the surface can be treated as the summation of returns from many independent scattering “patches”, each with a different range delay and Doppler shift [9], [16]. It is assumed that each patch is large relative to the correlation length of the surface, but sufficiently small so the the Doppler shift and slant range do not vary significantly over its dimensions. The echo return from the i th scattering patch is expressed as

$$R_i(t) = \xi_i \sqrt{\sigma_i^o} C B_i(t) e^{j2\pi[f_c + f_{dc} + f_{d,i} + \frac{1}{2}\mu(t - t_{d,i})](t - t_{d,i}) + \phi_i}. \quad (4)$$

Here, σ_i^o is the backscattering cross section at the scattering patch, ξ_i is a uni-variant Rayleigh random variable for the signal amplitude due to fading, ϕ_i is a uniform random variable (over $0 - 2\pi$) for the random phase of the return from the patch, $f_{d,i}$ is the Doppler shift of the patch, and $t_{d,i}$ is the round trip flight time to the patch given by $t_{d,i} = \frac{2r_i}{c}$ where r_i is the slant range to the patch.

The value C in (4) is defined such that

$$C^2 = \left(\frac{\lambda^2}{(4\pi)^3} \right) \left(\frac{E_t G_r G_p^2}{L_{sys}} \right), \quad (5)$$

where λ is the transmit wavelength, G_r is the receiver gain, G_p is the peak antenna gain, and L_{sys} is total two-way system loss. The echo return is windowed by the function $B_i(t)$

$$B_i(t) = p(t - t_{d,i}) \left(\frac{\delta A_i}{r_i^4} \right)^{\frac{1}{2}} [g_i(t) g_i(t - t_{d,i})]^{\frac{1}{2}}, \quad (6)$$

where δA_i is the area of the scattering patch, and $g_i(t)$ is the normalized antenna pattern gain in the direction of the i th scattering patch at time t . The term $g_i(t) g_i(t - t_{d,i})$ reflects the fact that the antenna gain is changing as a function of time as the antenna rotates.

The composite return over the entire footprint, $R(t)$, is given by

$$R(t) = \sum_{i \in \mathcal{F}} R_i(t), \quad (7)$$

where the summation is over all contiguous, unique patches in the illuminated region \mathcal{F} . (In this analysis, discrete summation over the illuminated region, rather than the more conventional integral representation, is used for clarity and to reflect the fact that X is evaluated numerically).

At the receiver, the signal is downconverted and deramped by multiplying $R_i(t)$ with

$$M(t) = \exp\{-2\pi j[\frac{1}{2}\mu(t - t_g)](t - t_g)\}, \quad (8)$$

where t_g is the reference delay, to yield

$$R_d(t) = R(t)M(t) = C \sum_{i \in \mathcal{F}} \xi_i \sqrt{\sigma_i^o} B_i(t) \exp\{2\pi j f_{b,i} t + j\psi_i\}. \quad (9)$$

Here, $f_{b,i}$ is the baseband frequency of the return from the i th patch and is given by

$$f_{b,i} = f_{d,i} + f_{dc} + \mu(t_g - t_{d,i}). \quad (10)$$

The new phase term ψ_i is a function of ϕ_i but is still a random variable uniformly distributed over $(0 - 2\pi)$. Examining Eq. (9) and Eq. (10) it is evident that the deramped echo is a composite of many scaled, windowed, single frequency tones with random phase. Each tonal frequency is determined by the range delay *and* Doppler shift associated with each scatterer. Note, then, that the processing does not represent pure range filtering because the iso-baseband frequency lines on the surface will be somewhat tilted with respect to the iso-range lines, the magnitude of the tilt being a function of the chirp rate μ .

The deramped signal is then digitally sampled and gated to form the sequence, $d[n]$

$$d[n] = C \sum_{i \in \mathcal{F}} \xi_i \sqrt{\sigma_i^o} G(t_n) B_i(t_n) \exp\{2\pi j f_{b,i}(t_n) + j\psi_i\}. \quad (11)$$

Here, the sample time, t_n , is equal to $t_{gs} + nT$, where t_{gs} is the time associated with the first sample input to the DFT, n is the sample number, and T is the sample period. $G(t)$ is a rectangular window function representing the range gate ($G = 1$ for signal “on” or $G = 0$ for signal “off”).

To form the slice measurement P_s^j , a DFT is applied to the sample sequence, the Fourier domain sequence is magnitude squared, and then the appropriate periodogram bins are summed. Also, we assume that the backscatter cross section is constant over the slice to obtain

$$P_s^j = \sigma^o C^2 \sum_{k=k_s}^{k_e} \left| \sum_{n=0}^{N-1} \left[\sum_{i \in \mathcal{F}} \xi_i G(t_n) B_i(t_n) \exp\{2\pi j f_{b,i}(t_n) + j\psi_i\} \right] \exp\{-2\pi j \frac{kn}{N}\} \right|^2, \quad (12)$$

where k_s and k_e are the slice start and end bin numbers and N is the total number of samples input to the DFT (FFT size).

Because P_s^j is random quantity, we must take the expected value to find X :

$$\mathcal{E}[P_s^j] = \sigma^o C^2 \sum_{k=k_s}^{k_e} \sum_{i \in \mathcal{F}} \left| \sum_{n=0}^{N-1} G(t_n) B_i(t_n) \exp\{2\pi j(f_{b,i}T - \frac{k}{N})n\} \right|^2, \quad (13)$$

where, to eliminate the random variables and reorder the summations, we have utilized the assumption that separate scattering patches are uncorrelated (i.e. that $\mathcal{E}[e^{j\psi_m} e^{-j\psi_n}] = 0$ for $m \neq n$), and that ξ is univariant. Referring to Eq. (2), we conclude that

$$X = C^2 \sum_{k=k_s}^{k_e} \sum_{i \in \mathcal{F}} \left| \sum_{n=0}^{N-1} G(t_n) B_i(t_n) \exp\{2\pi j(f_{b,i}T - \frac{k}{N})n\} \right|^2. \quad (14)$$

Equation (14) is a general expression for X for a rotating antenna with digital range filtering.

Under certain conditions (which apply in the case of *Sea Winds*) the computation of X may be simplified somewhat. If the transmit pulse envelope is rectangular, we can write

$$\begin{aligned} p(t) &= \frac{1}{\sqrt{T_p}} \quad \text{for } t_{ps} \leq t < t_{ps} + T_p \\ p(t) &= 0 \quad \text{otherwise} \end{aligned} \quad (15)$$

where t_{ps} is the time of transmit pulse start. If we further assume that the antenna gain in the direction of a given surface patch is constant during the pulse period, we can also write

$$B_i(t_n) = p(t_n - t_{d,i}) \left(\frac{\delta A_i}{r_i^4} \right)^{\frac{1}{2}} [g_i(t_{trs}) g_i(t_{rec})]^{\frac{1}{2}}, \quad (16)$$

where $g_i(t_{trs})$ is the gain in the direction of the i th patch at the time of transmit, and $g_i(t_{rec})$ is the gain in the direction of the i th patch at the time of receive after the antenna has rotated during the pulse round-trip flight time $t_{d,i}$. The above two assumptions are equivalent to assuming that the the echo return from a given scatterer is flat, and is not modulated by either the pulse envelope or the rotating antenna beam. The sampled signal values will thus correspond to a rectangular window whose length is determined by the overlap between the delayed return pulse and the range gate window.

Employing Eq. (15) and Eq. (16), Eq. (14) can be written as

$$X = \frac{C^2}{T_p} \sum_{k=k_s}^{k_e} \sum_{i \in \mathcal{F}} \left(\frac{\delta A_i g_i(t_{trs}) g_i(t_{rec})}{r_i^4} \right) \left| \sum_{n=n_{s,i}}^{n_{s,i} + N_{p,i}} \exp\{2\pi j(f_{b,i}T - \frac{k}{N})n\} \right|^2. \quad (17)$$

Here, $n_{s,i}$ is the sample in the sequence $d[n]$ associated with the leading edge of the gated echo from the i th patch. $N_{p,i}$ is the length of the echo from the i th patch (given in number of samples) captured by the range gate. $N_{p,i}$ is given by

$$N_{p,i} = \text{int} \left(T_p \sum_{n=0}^{N-1} p_r(t_n - t_{d,i}) G(t_n) \right). \quad (18)$$

It will be convenient, particularly for the analysis of measurement variance, to define the DFT term in Eq. (17) as the function β where

$$\beta(i, k) = \sum_{n=n_s}^{n_s+N_{p,i}} \exp\{2\pi j(f_{b,i}T - \frac{k}{N})n\}. \quad (19)$$

Evaluating Eq. (19) we have that

$$\beta(i, k) = \left(\frac{\exp[j\pi(N_{p,i} + 2n_{s,i})(f_{b,i}T - \frac{k}{N})]}{\exp[j\pi(f_{b,i}T - \frac{k}{N})]} \right) \left(\frac{\sin[\pi N_{p,i}(f_{b,i}T - \frac{k}{N})]}{\sin[\pi(f_{b,i}T - \frac{k}{N})]} \right). \quad (20)$$

Note that because the complex phase term for $|\beta(i, k)|^2$ cancels, we can always sum from 0 to $N_{p,i}$ in the DFT regardless of the pulse position in the range gate. Equation (17) then becomes,

$$X = \frac{C^2}{T_p} \sum_{i \in \mathcal{F}} \left\{ \left(\frac{\delta A_i g_i(t_{trs}) g_i(t_{rec})}{r_i^4} \right) \sum_{k=k_s}^{k_e} \left[\frac{\sin^2[\pi N_{p,i}(f_{b,i}T - \frac{k}{N})]}{\sin^2[\pi(f_{b,i}T - \frac{k}{N})]} \right] \right\}. \quad (21)$$

For clarity, Fig. 8 is provided to illustrate the integration over the scattering patches. Using Eq. (21), X for a sample slice is plotted versus orbit position and antenna azimuth angle for the expected *Quikscat* orbit in Fig. 9. Note that the value of X varies significantly, necessitating an adjustment as a function of orbit position and antenna azimuth to maintain calibration accuracy. Despite the simplifications embodied in Eq. (21), X is still too computationally expensive to compute repeatedly for each individual pulse during ground data processing. Where the satellite orbit is very stable, as is expected for both the *Quikscat* and *ADEOS-II* spacecraft, X may be precomputed in tabular form which is then interpolated in azimuth and orbit position to obtain values for each pulse and slice.

Spatial Response Function and Surface Sampling

It is insightful to view the X parameter is as an integration of the instrument spatial response function on the Earth's surface. The spatial response function can be constructed

from Eq. (21) by taking the energy contribution to the slice from each scattering patch, and then normalizing by the area of the patch. Denoting this function as S , we have

$$S(\vec{l}_i) = \frac{C^2 g_i(t_{trs}) g_i(t_{rec})}{T_p r_i^4} \sum_{k=k_s}^{k_e} \left[\frac{\sin^2[\pi N_{p,i}(f_{b,i}T - \frac{k}{N})]}{\sin^2[\pi(f_{b,i}T - \frac{k}{N})]} \right], \quad (22)$$

where \vec{l}_i is the surface position (in latitude and longitude, for instance) of the i th patch.

In Fig. 10 the spatial response function is displayed for two cases. In Fig. 10(a), the response for the beam-limited case (no range filtering) is shown. In Fig. 10(b), the response for an example range slice of width 7 km ($B_s = 8.3$ kHz for $\mu = 250$ kHz/ms) is shown. In Fig. 10(b), note the sharp drop-off of the response function in the range direction. Such a sharp edge in the spatial response preserves high frequency information in the spatial frequency domain, and thus is a highly desirable property for enhanced resolution image reconstruction purposes. Note also the tilt in the orientation of the slice due to Doppler shift across the footprint. In Fig. 11, the surface sampling achieved by the center eight slices for several consecutive pulses is shown. Here the σ° cell outlines are delineated by plotting the approximate 3 dB contour of the slice response. As is evident, the measurements form a very dense sampling of the surface with many overlapping cells, which again is favorable for ERI as well as higher resolution wind retrieval.

Errors in X

Regardless of the care taken in deriving an expression for X , the calibration accuracy can only be as good as our knowledge of the various instrumental and geometric parameters comprising X . The parameter C in Eq. (5) embodies all radiometric components of X . Although there is potential for error in determining the value of C , this error is likely to be a constant bias for all measurements and should not contribute significantly to relative calibration error. This is because the determination of transmit power and receiver gain through periodic “loop-back” calibration measurements relies on a very stable, thermally controlled waveguide coupler. Furthermore, the antenna gain and system losses are likewise expected to be quite constant because of reliance on equally stable passive RF components. What can change on-orbit, however, is the measurement geometry, primarily through variations in the spacecraft attitude. In fact, attitude knowledge errors were observed to constitute the dominant source of relative calibration error for both the SEASAT-A and NSCAT

scatterometers [5],[15].

As the attitude changes, the antenna pattern shifts with respect to the lines of constant baseband frequency on the Earth which form the slice edges. If the attitude change is unknown, an error in X , and consequently an error in σ° , will result. The magnitude of this error can be evaluated by taking the ratio of X calculated at the true attitude to the estimated attitude. In general, we are much more sensitive to attitude changes that effect the elevation angle of the antenna pointing (spacecraft pitch and roll) as opposed to changes that effect the azimuth angle (spacecraft yaw). In Fig. 12, the error in σ° is plotted vs. the error in elevation angle for different slices. The slices are numbered according to their position in the antenna beam: slice 1 being an “inner” slice near the peak of the antenna pattern as projected on the surface, and slice 5 an “outer” further down on the main beam. It is evident that slices near the peak where the antenna pattern is varying slowly are relatively insensitive to changes in pointing, whereas the outer slices where the pattern is changing rapidly are quite sensitive to pointing errors. This, then, becomes a key design consideration for improved resolution measurements that did not exist for the low resolution case. To achieve the highest desired calibration accuracy for all slices requires spacecraft pointing knowledge on the order of 0.01 degrees. Less ambitious designs for the spacecraft attitude determination system implies that calibration goals may still be achieved for the innermost slices.

B. Backscatter Measurement Variance

As mentioned in Section II, measurements of the detected energy, P_s^j , are “noisy” due to radar fading and the presence of system thermal noise. Unlike calibration error, which is essentially deterministic and can be improved by better knowledge of instrument parameter values and pointing, the random variations in P_s^j place a fundamental limit on the instrument precision. For the selected range filtering implementation, however, we may optimize measurement precision by careful selection of the transmit chirp rate and slice bandwidth. This section presents the various equations necessary to perform this optimization, and discusses results for the SeaWinds design.

K_p Parameter

Previous studies have addressed in detail the issue of measurement variance for fan-beam systems with Doppler filtering [2], and pencil-beam systems with transmit modulation and square-law detection [9]. Here the analysis specific to a pencil-beam scatterometer with linear chirp modulation and digital range filtering is outlined.

In scatterometry it has become customary to define the measurement error in terms of the so-called K_p parameter

$$K_p = \frac{\sqrt{\text{Var}[\sigma^o]}}{\mathcal{E}[\sigma^o]} = \frac{\sqrt{\text{Var}[P_s]}}{\mathcal{E}[P_s]}, \quad (23)$$

where the slice index “ j ” has been dropped for notational simplicity. K_p is then the normalized standard deviation of the measurement error, or percentage error. A goal of scatterometer design is the minimization of K_p . From Eq. (1), we can write the variance of P_s^j as

$$\text{Var}[P_s] = \text{Var}[C_{sn}] + \text{Var}[P_n] + 2(\mathcal{E}[C_{sn}]\mathcal{E}[P_n] - \mathcal{E}[C_{sn}P_n]). \quad (24)$$

As is shown in [9], when $B_n \gg B_s$, the second and third terms of Eq. (24) are much smaller than $\text{Var}[C_{sn}]$. For *ScaWinds*, because $B_n = 1$ MHz and $B_s = 8.3$ kHz, this condition applies and allows us to assume

$$K_p = \frac{\sqrt{\text{Var}[C_{sn}]}}{\mathcal{E}[P_s]}. \quad (25)$$

Because the derivation of $\text{Var}[C_{sn}]$ is somewhat involved, only the major assumptions and results are discussed here. The derivation procedure is more similar to the development described in [9], which employs time domain techniques, rather than [2] which employs a frequency domain approach. This is to insure that the resultant expression is sufficiently general to handle the case where the echo return can not be modeled accurately as a stationary random process. Noting that C_{sn} can be written as

$$C_{sn} = C^2 \sum_{k=k_s}^{k_e} \left| \sum_{n=0}^{N-1} (d[n] + \nu[n])e^{-2\pi j \frac{kn}{N}} \right|^2, \quad (26)$$

where $d[n]$ is the signal sequence as described in Eq. (11) and $\nu[n]$ is the noise sequence, the necessary expectations of squared terms and associated cross products are then taken. Making the very reasonable assumption that both signal and noise voltage terms are Gaussian distributed, a familiar expansion for the fourth order moment of Gaussian random

variables is employed [9]. Further assuming that the return echo from a given scatterer has a rectangular envelope – the same assumption that was made to develop Eq. (21) – it can be shown that

$$K_{pc}^2 = A + \frac{B}{SNR} + \frac{C}{SNR^2}. \quad (27)$$

Here, SNR is the signal-to-noise ratio for the slice and is defined as

$$SNR = \frac{X\sigma^o}{T_g B_s N_0}, \quad (28)$$

where T_g is the range gate length and N_0 is the noise floor power spectral density expressed in suitable units. The parameters A , B , and C can be shown to be

$$\begin{aligned} A &= \frac{1}{X^2} \sum_k \sum_h \sum_i \sum_l c_i^2 c_l^2 \beta(i, k) \beta^*(i, h) \beta^*(l, k) \beta(l, h) \\ B &= \frac{2}{K N_\nu X} \sum_k \sum_h \sum_i c_i^2 \frac{e^{j\pi \frac{(k-h)}{N} (N_\nu + 2n_\nu)} \sin(\pi \frac{(k-h)}{N} N_\nu)}{e^{j\pi \frac{(k-h)}{N} \sin(\pi \frac{(k-h)}{N})}} \beta(i, k) \beta^*(i, h) \\ C &= \frac{1}{K^2 N_\nu^2} \sum_k \sum_h \sum_{n=0}^{N_\nu-1} \sum_{m=0}^{N_\nu-1} e^{j\frac{2\pi}{N} (k-h)(m-n)} \end{aligned} \quad (29)$$

where $\beta(i, k)$ is as defined in Eq. (20), n_ν is the sample number in $d[n]$ corresponding to the opening of the range gate, N_ν is the duration (in number of samples) of the range gate open time, K is the total number of periodogram bins summed to form the slice, and c_i is defined as

$$\frac{C^2 \delta A_i g_i(t_{trs}) g_i(t_{rec})}{T_p r_i^4}. \quad (30)$$

Equation (29) can be approximated by a form more suited to intuitive analysis by making the following three assumptions: 1) the echo return is nearly stationary – i.e. the pulse length T_p (1.5 ms for *SeaWinds*) is much greater than the time it takes the fill the entire antenna beam (about 0.5 ms for *SeaWinds*), 2) $B_{3dB} \gg B_s$, and 3) $T_p B_s \gg 1$. Under these conditions, which apply for *SeaWinds*, we can approximate A , B , and C as

$$\begin{aligned} A &= \frac{1}{B_s T_p} \\ B &= \frac{2}{B_s T_g} \\ C &= \frac{1}{B_s T_g}. \end{aligned} \quad (31)$$

Taking Eq. (31) together with Eq. (27) and Eq. (28), we obtain insight into the design considerations necessary to minimize K_p . The “ A ” term is the contribution to the variance

due to radar signal fading alone, with $B_s T_p$ approximating the number of independent “looks” associated with a given measurement slice. Assuming that T_p is fixed due to timing and sampling constraints, we can thus reduce A by increasing the bandwidth of the slice measurement, B_s . The slice bandwidth is, in turn, related to the narrow (range) dimension of the slice spatial response on the surface and the transmit chirp rate. For the *ScaWinds* orbit altitude of 800 km,

$$B_s \approx W \sqrt{2 \times 10^{-5} \mu^2 + 0.14} \quad (32)$$

where B_s is the slice bandwidth in kHz, μ is the transmit pulse chirp rate in kHz/ms, and W is the mean range dimension of the slice in km. Thus, for a given slice dimension we can increase the bandwidth by increasing the chirp rate.

A trade-off exists, however, because as B_s is increased, SNR decreases (see Eq. (28)), and the B and C terms of Eq. (27) get larger. In other words, we must balance the benefits of a larger measurement bandwidth with the effects of allowing more thermal noise to enter the measurement. A similar trade-off analysis was performed for the previous beam-limited *ScaWinds* design (outlined in [13]). Proceeding along similar lines, a chirp rate of $\mu = 250$ kHz/ms was selected for the new design with range filtering. This value was found to strike a balance in performance for high wind speeds – which have high inherent SNR (> 6 dB) and hence benefit from larger measurement bandwidths – and low wind speeds – which have low SNR (< 0 dB) where the variance may be made worse by increasing the measurement bandwidth.

IV. Enhanced Resolution Imaging Performance

As previously noted, Ku-band scatterometer σ° measurements have proved to be very useful in land and ice studies; hence the desire to maintain a long time series of such measurements. While the original design of *ScaWinds* would have provided usable measurements, the modified design will provide σ° measurements with significantly improved resolution. This is expected to expand the utility of the *Scawinds* measurements in land/ice science studies as well as in the primary wind observation mission. In this section the land/ice imaging resolution of the original and modified *Scawinds* designs are compared using conventional gridding and a particular ERI technique known as the Scatterometer Image Reconstruction

with Filtering (SIRF) [7]. This analysis illustrates the benefits of adding range filtering capability to the *ScaWinds* design.

To make the performance comparison, both beam-limited and range sliced σ° cells are used. Simulated backscatter measurements are generated with the aid of a synthetic image of the surface σ° (see Fig. 13(a)), which is similar to that used in [7]. For each beam-limited footprint or range slice, the effective σ° measurement is computed as the weighted average of the pixels of the synthetic image where the weighting is the spatial response function described earlier. Then, K_p is computed and Monte Carlo noise is added to generate a simulated noisy σ° measurement. For this analysis, calibration errors were neglected.

In order to simulate the Earth location and orientation of the measurements, the synthetic test image was located over Wilkes Land in Antarctica. The test region is approximately $1000 \text{ km} \times 800 \text{ km}$ and is centered at 74.5° S and 128.5° W . Over a one day period, at least part of the test site is observed during 5 passes of *QuikScat*. The imaging results for a number of cases are compared in Fig. 13. Using the simulated σ° measurements, images were computed using a (non-enhanced) gridding approach and the SIRF resolution enhancement technique for both beam-limited cells and slices. The non-enhanced grid images have a pixel resolution of approximately 25 km while the SIRF images have a pixel resolution of approximately 4.5 km.

To generate the non-enhanced images, each σ° measurement is assigned to the grid element in which its center falls. The average σ° is then computed and assigned to the associated pixel. The SIRF images were generated with a modified form of the SIRF algorithm. While the original SIRF algorithm (described in [7]) is bi-variate, estimating both the incidence angle normalized σ° and the incidence angle dependence of σ° , the algorithm used here is modified to image only σ° , similar to the radiometer version of the algorithm [10].

Subjectively, the addition of range resolution capability is observed to significantly improve the effective two dimensional resolution of land/ice images produced from the simulated Seawinds measurements whether or not resolution enhancement is applied. This is true, even though range filtering resolves the footprint in just one dimension, because of the different orientations σ° cells contributing to each pixel. Using the SIRF algorithm further improves the image resolution over the gridding approach. Because the SeaWinds

measurements densely overlap, reasonable images can be made from only one day of data in this polar region. However, the noise level in the images can be reduced if multiple days are combined and the surface is temporally stable.

V. Conclusions

From the results of the preceding section, it is clear that the resolution performance of a scanning pencil-beam scatterometer can be significantly improved by the addition of a range filtering scheme. Interestingly, this is the case even though range filtering resolves the antenna footprint in one dimension. Resolution in a second dimension occurs as the range slices are collected and used with an enhanced resolution imaging algorithm to solve for the underlying backscatter. Range “slicing” of the antenna footprint is thus a low-cost way of extending the capabilities of small, scanning pencil-beam scatterometers such as *SeaWinds*.

As discussed, range filtering is generally preferred over Doppler filtering because of superior measurement variance performance and more favorable geometrical orientation of the σ^0 cells. Although range discrimination by deramp processing is a familiar and relatively straightforward approach, its implementation must be accompanied by a careful analysis of calibration issues in order to meet backscatter measurement accuracy goals. This includes a formulation of the radar equation which includes digital processing and antenna rotation effects, as well as a consideration of spacecraft attitude variations. Trade-offs to obtain minimum measurement variance by optimizing the chirp rate and detection bandwidth for the available signal-to-noise ratio must also be performed.

V. Summary

Flights of the *SeaWinds* instrument in 1998 and 2000 form the foundation of the NASA Ku-band scatterometer program into the next century. In this paper, the new design for *SeaWinds* resolution processing has been described. As demonstrated, the spatial resolution performance of *SeaWinds* has been significantly improved by the addition of a range filtering scheme. This will be particularly useful for land and ice images constructed using enhanced resolution imaging algorithms. Range slicing of the antenna footprint, coupled with the application of ERI, is thus an economical way of extending the capabilities of small, scanning pencil-beam scatterometers such as *SeaWinds*.

As discussed, range filtering is generally preferred over Doppler filtering because of superior measurement variance performance and more favorable geometrical orientation of the σ° cells. Although range discrimination by deramp processing is a relatively straightforward approach, its implementation must be accompanied by a careful accounting of geometric calibration factors in order to meet backscatter measurement accuracy goals. This involves a formulation for the radar equation which includes digital processing and antenna rotation effects, as well as a consideration of spacecraft attitude variations. Trade-offs to obtain minimum measurement variance by optimizing the chirp rate and detection bandwidth for the available signal-to-noise ratio must also be conducted to obtain the best performance.

Acknowledgments

The research described in this paper was carried out by the Jet Propulsion Laboratory, California Institute of Technology, under a contract with the National Aeronautics and Space Administration.

Appendix A: Calculating P_n^j

As discussed in Section II, to determine σ^o from each measurement “slice” we must first subtract off the thermal noise energy component, P_n^j . To determine P_n^j , we use both the “noise-only” processor output, C_{no} , and the sum of all the slice measurements, C_{sn}^e , where $C_{sn}^e = \sum_1^{12} C_{sn}^j$.

To insure that the thermal noise estimate corresponds to the same surface scene observed during the slice measurement, the “noise-only” and “signal+noise” processing operations are gated simultaneously (see [13]). Thus we have

$$\begin{aligned} C_{no} &= g_n(E + B_n T_g N_0) \\ C_{sn}^e &= g_e(E + B_e T_g N_0), \end{aligned} \quad (1)$$

where g_n and g_e are the receiver gains through the “noise-only” and “signal+noise” processing paths respectively, E is the total echo energy captured during gate time T_g , B_n and B_e are the effective bandwidths of the two measurements (see Fig. 7), and N_0 is the thermal noise power spectral density. Here it is assumed that B_e is sufficiently wide to pass all the deramped echo power spectrum.

Eliminating E and solving for $g_e T_g N_0$ we obtain

$$g_e T_g N_0 = \left(\frac{1}{B_e} \right) \frac{\frac{g_e}{g_n} C_{no} - C_{sn}^e}{\frac{B_n}{B_e} - 1}, \quad (2)$$

which is the total thermal noise contribution in the bandwidth B_e . Note that to get this result we needed only the ratio of the gains in the two channels not their absolute values. Because we know $\frac{B_n}{B_e}$ we can obtain

$$P_n^j = B_s^j g_e T_g N_0. \quad (3)$$

References

- [1] E.P.W. Attema, "The Active Microwave Instrument On-Board the ERS-1 Satellite," *Proceedings of the IEEE*, pp. 791-799, Vol. 79, No. 6, June 1991.
- [2] C-Y Chi, D.G. Long, F.K. Li, "Radar Backscatter Measurement Accuracies Using Digital Doppler Processors in Spaceborne Scatterometers," *IEEE Trans. on Geoscience and Remote Sensing*, Vol. GE-24, May 1986.
- [3] M.H. Freilich, D.G. Long and R.S. Dunbar, "NSCAT Measurement of Wind Wakes and Jets Near South Georgia Island," submitted to *Science*, 1998.
- [4] J.E. Graf, W-Y Tsai, and W.L. Jones, "Overview of QuikSCAT Mission- A Quick Deployment of a High Resolution, Wide Swath Scanning Scatterometer for Ocean Wind Measurement," *Southeastcon'98*, April 1998, Orlando, FL.
- [5] Johnson, J.W., et al., "SEASAT-A Satellite Scatterometer Instrument Evaluation," *IEEE J. Oceanic Eng.*, OE-5, 1980.
- [6] W.L. Jones, V.J. Cardone, W.J. Pierson, J. Zec, L.P. Rice, A. Cox, and W. B. Sylvester, "NSCAT High Resolution Surface Winds Measurements in Typhoon Violet," accepted for pub. *JGR - Oceans (Special NSCAT issue)*.
- [7] D.G. Long, P.J. Hardin, and P.T. Whiting, "Resolution Enhancement of Spaceborne Scatterometer Data," *IEEE Transactions on Geoscience and Remote Sensing*, Vol. 31, No. 3, pp. 700-715, May 1993.
- [8] D. G. Long and P. Hardin, "Vegetation Studies of the Amazon Basin Using Enhanced Resolution Seasat Scatterometer Data," *IEEE Transactions on Geoscience and Remote Sensing*, Vol. 32, No. 2, pp. 449-460, Mar. 1994.
- [9] D.G. Long and M.W. Spencer, "Radar backscatter measurement accuracy for a spaceborne pencil-beam wind scatterometer with transmit modulation," *IEEE Transactions on Geoscience and Remote Sensing*, Vol 35, No. 1, pp. 102-114, Jan. 1997.
- [10] D.G. Long, and D.L. Daum, "Spatial Resolution Enhancement of SSM/I Data," *IEEE Transactions on Geoscience and Remote Sensing*, Vol. 35, No. 2, pp. 407-417, 1998.

- [11] D.G. Long and M.R. Drinkwater, "Cryosphere Studies Using NSCAT Data," Invited paper, in press, *IEEE Transactions on Geoscience and Remote Sensing*, 1998.
- [12] F. Naderi, M.H. Freilich, and D.G. Long, "Spaceborne Radar Measurement of Wind Velocity Over the Ocean—An Overview of the NSCAT Scatterometer System," *Proceedings of the IEEE*, pp. 850-866, Vol. 79, No. 6, June 1991.
- [13] M.W. Spencer, C. Wu, and D.G. Long, "Tradeoffs in the Design of a Spaceborne Scanning Pencil Beam Scatterometer: Application to SeaWinds," *IEEE Transactions on Geoscience and Remote Sensing*, Vol 35, No. 1, pp. 115-126, Jan., 1997.
- [14] J.N. Huddleston, W-Y Tsai, M.W. Spencer, and R. West, "Modeling and Simulation for SeaWinds 1-B System Design and Performance Evaluation," *Proceedings of SPIE: Sensors, Systems, and Next-Generation Satellites*, London, UK, September 1997.
- [15] W-Y Tsai, J.E. Graf, C. Winn, J.N. Huddleston, S. Dunbar, M.H. Freilich, F.J. Wentz, D.G. Long, W.L. Jones, "Post-Launch Sensor Verification and Calibration of the NASA Scatterometer," in press, *IEEE Transactions on Geoscience and Remote Sensing*, 1998.
- [16] F.T. Ulaby, R.K. Moore, and A.K. Fung, *Microwave Remote Sensing – Active and Passive*, Vol. 2, Reading, Mass: Addison-Wesley Publishing Company, 1981.
- [17] C. Wu, J. Graf, M. Freilich, D.G. Long, M. Spencer, W. Tsai, D. Lisman, and C. Winn, "The SeaWinds Scatterometer Instrument," *Proceedings of the International Geoscience and Remote Sensing Symposium*, Pasadena, California, August 8-12, pp. 1511-1515, 1994.
- [18] A.R. Zieger, D.W. Hancock, G.S. Hayne, C.L. Purdy, "NASA Radar Altimeter for the TOPEX/POSEIDON Project," *Proceedings of the IEEE*, Vol. 79, No. 6, June 1991.

Parameter	Inner Beam	Outer Beam
Polarization	H	V
Elevation Angle	40°	46°
Surface Incidence Angle	47°	55°
Slant Range	1100 km.	1245 km.
3 dB Beam Widths (az × el)	1.8° × 1.6°	1.7° × 1.4°
Two-Way 3 dB Footprint Dimensions (az × el)	24 × 31 km	26 × 36 km
Peak Gain	38.5 dBi	39 dBi
Rotation Rate	18 rpm	
Along Track Spacing	22 km.	22 km.
Along Scan Spacing	15 km.	19 km.

Table 1: *SeaWinds* Antenna and Measurement Geometry Parameters

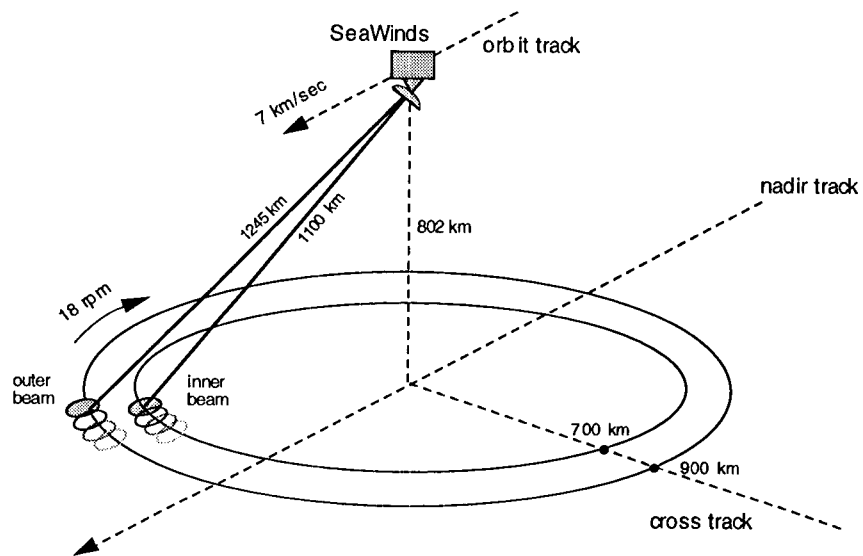


Figure 1: *SeaWinds* measurement geometry.

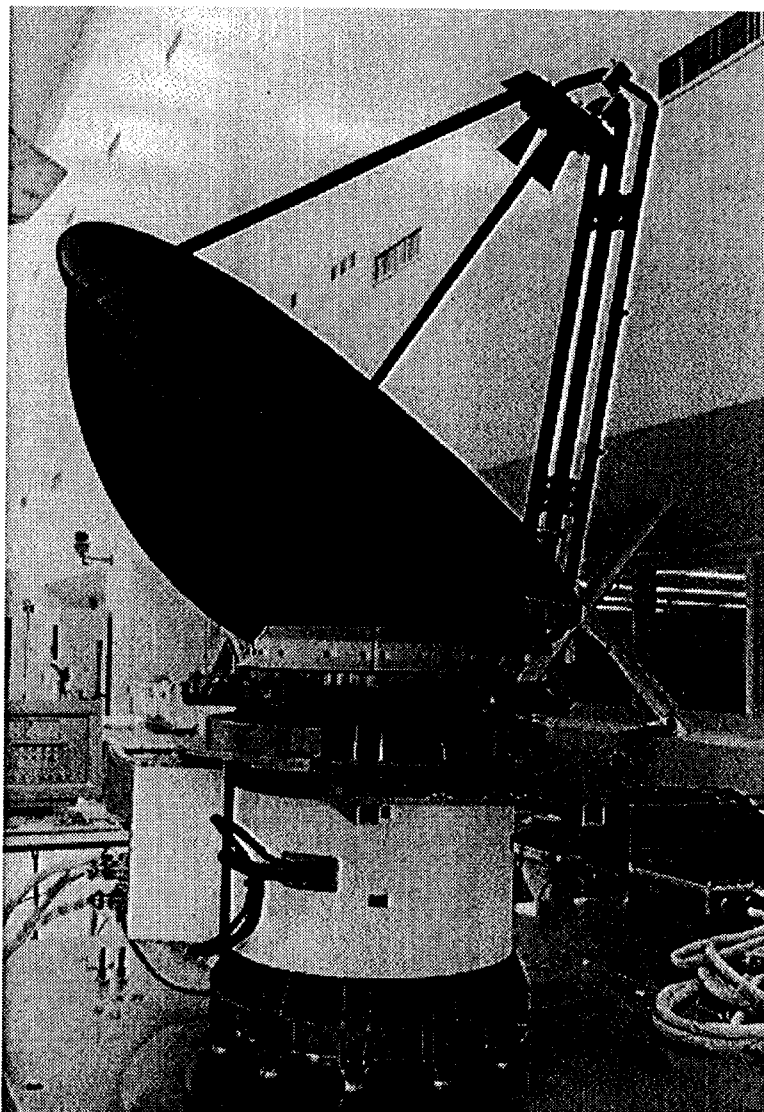


Figure 2: *SeaWinds* antenna and rotary mechanism. (Photo to be provided at time of final paper submission).

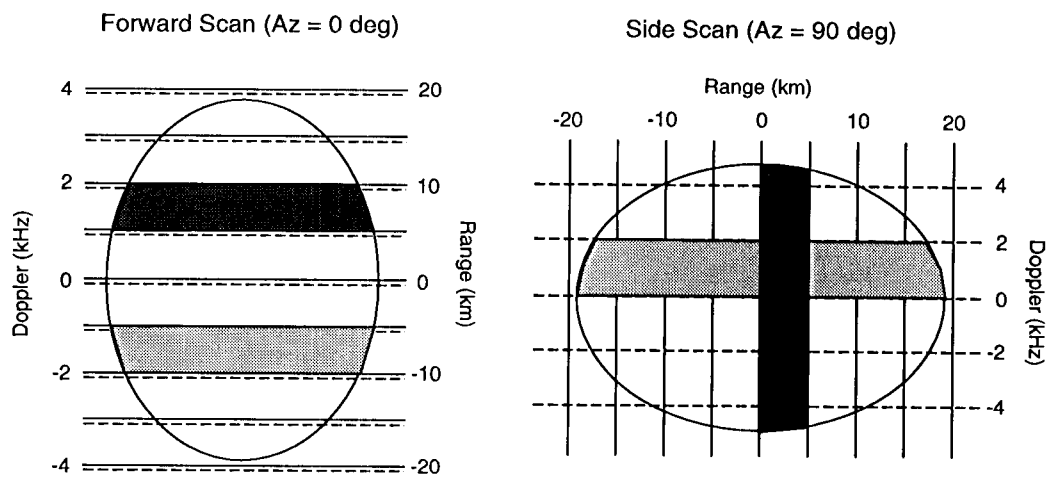


Figure 3: Conceptual diagram of *SeaWinds* 3 dB antenna footprint projected on the surface (oval) with two-way iso-range (solid) and iso-Doppler (dashed) lines. Shaded areas illustrate range filtered (dark) and Doppler filtered (light) resolution elements.

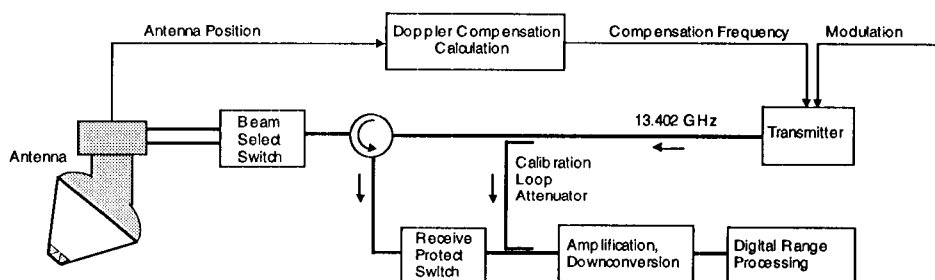


Figure 4: Block diagram of *SeaWinds* radar system.

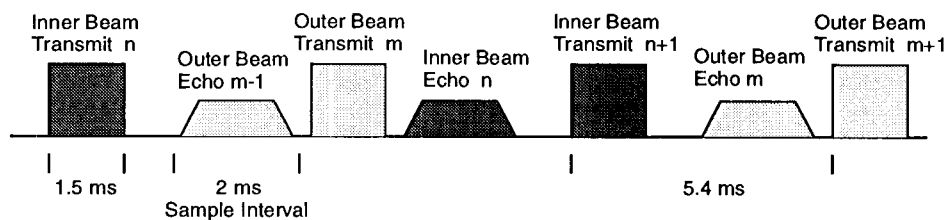


Figure 5: *SeaWinds* transmit and receive timing. Note that pulses alternate between inner and outer beam, with two pulses in flight.

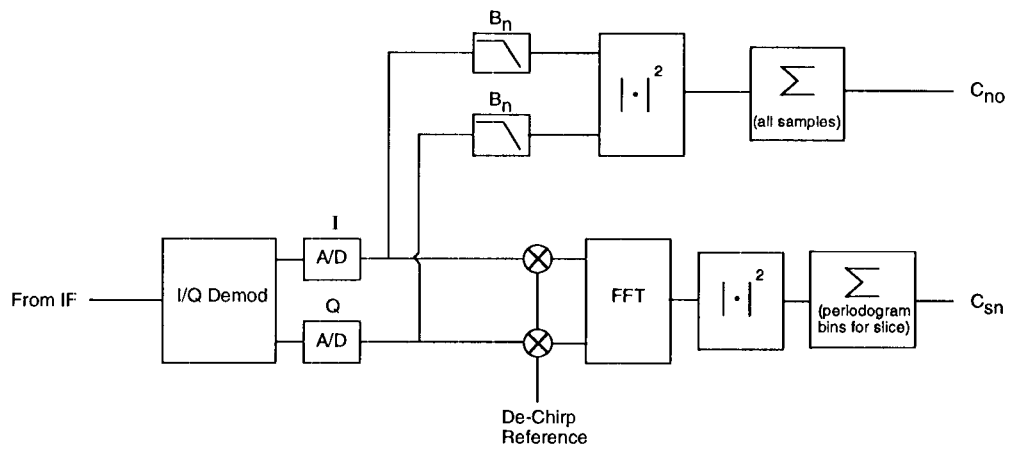


Figure 6: Functional diagram of *SeaWinds* digital range processing and “noise-only” processing.

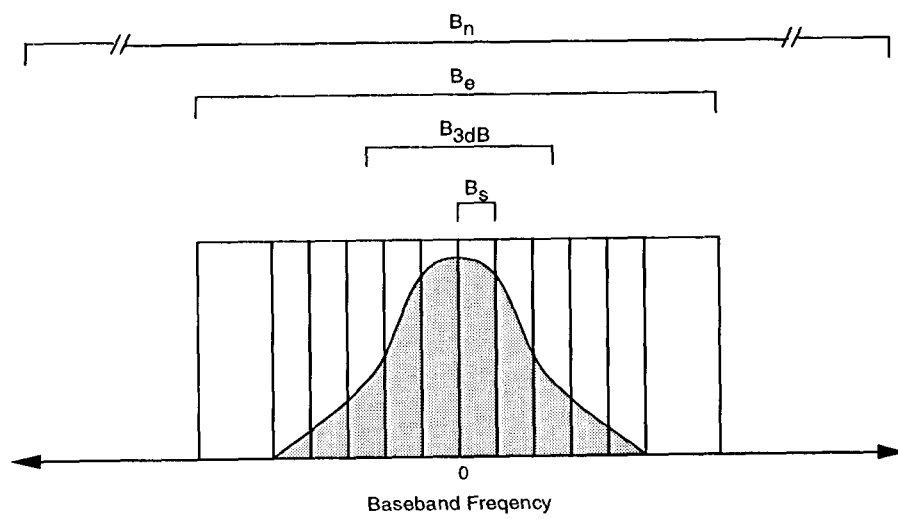


Figure 7: Conceptual diagram illustrating de-ramped echo spectrum (shaded), range slices, and other bandwidths used in processing.

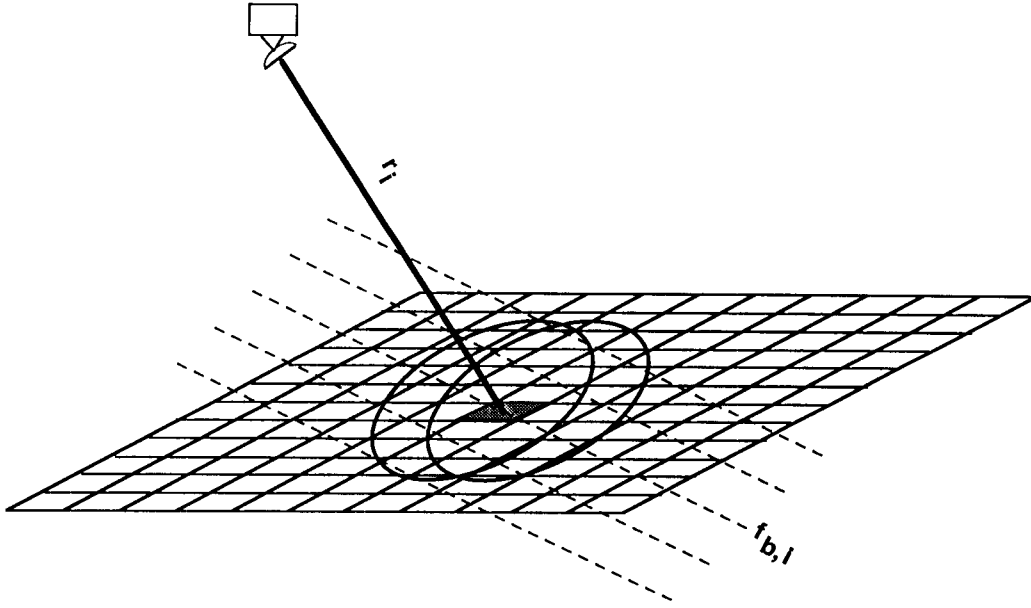


Figure 8: X parameter calculation geometry. Shaded region represents i th surface element with incremental area δA_i . Dotted lines represent lines of constant base-band frequency, with baseband frequency of i th element $f_{b,i}$. Offset ovals represent antenna footprint position at time of transmit and receive. Range from i th element to sensor is r_i .

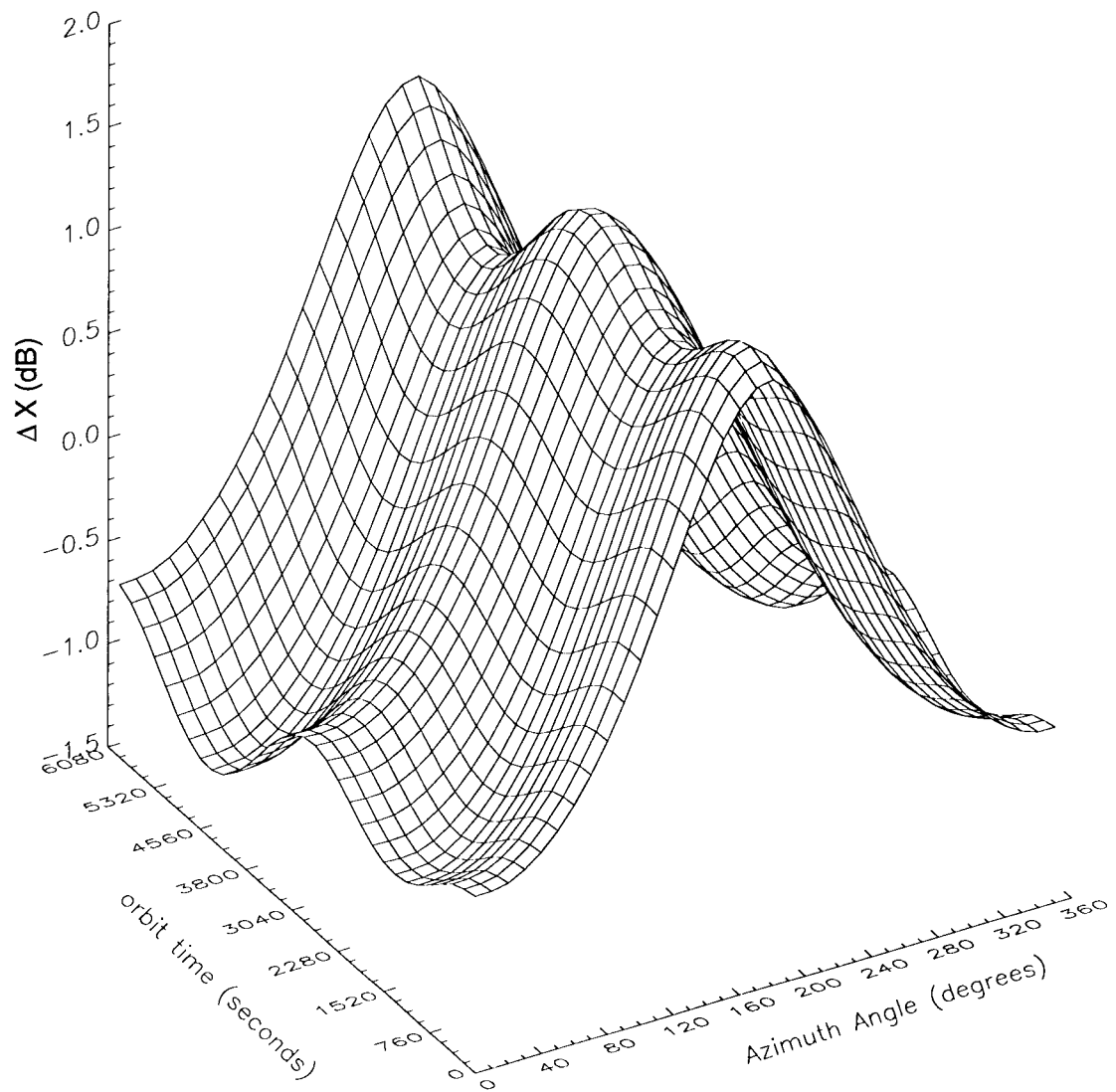
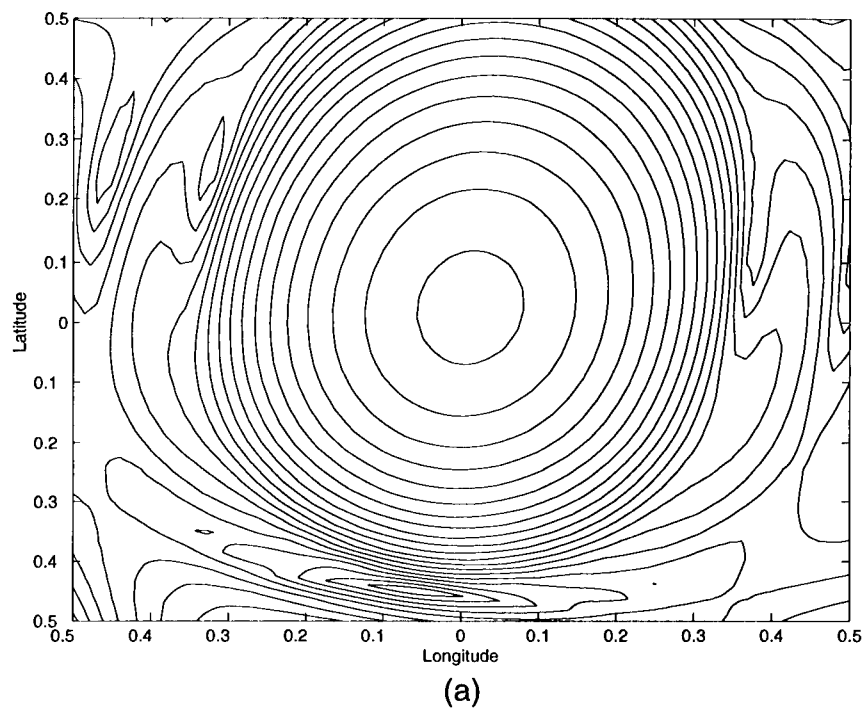


Figure 9: X parameter for example “slice” vs. orbit time (one complete orbit = 6080 seconds) and antenna scan azimuth angle. Here X has been normalized by its mean value.



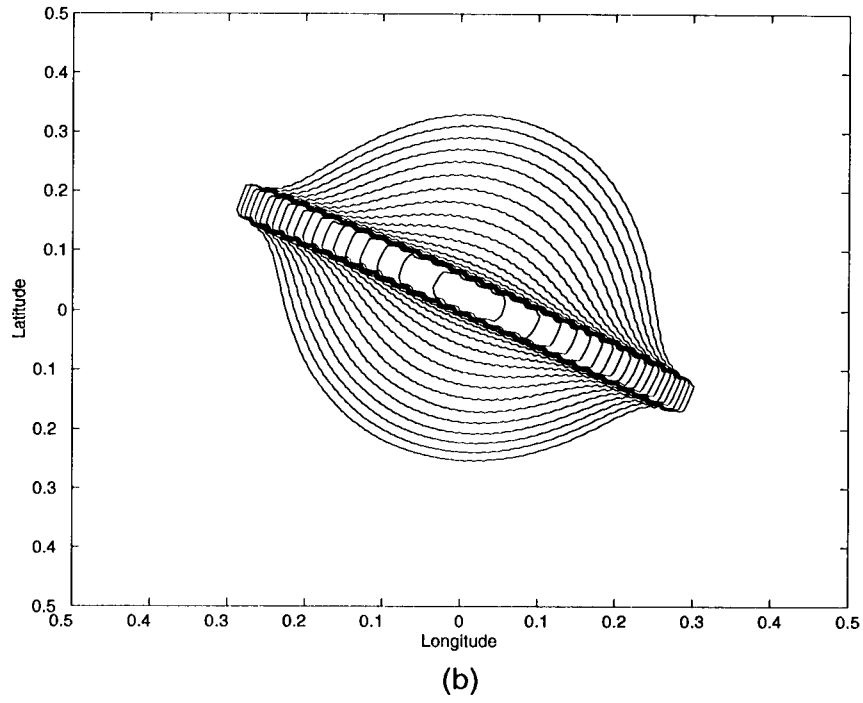


Figure 10: (a) Example inner beam σ^o cell spatial response for beam-limited (no range filtering) case. (b) Example inner beam σ^o cell spatial response for center range slice. Contours spacing at 1 dB intervals.

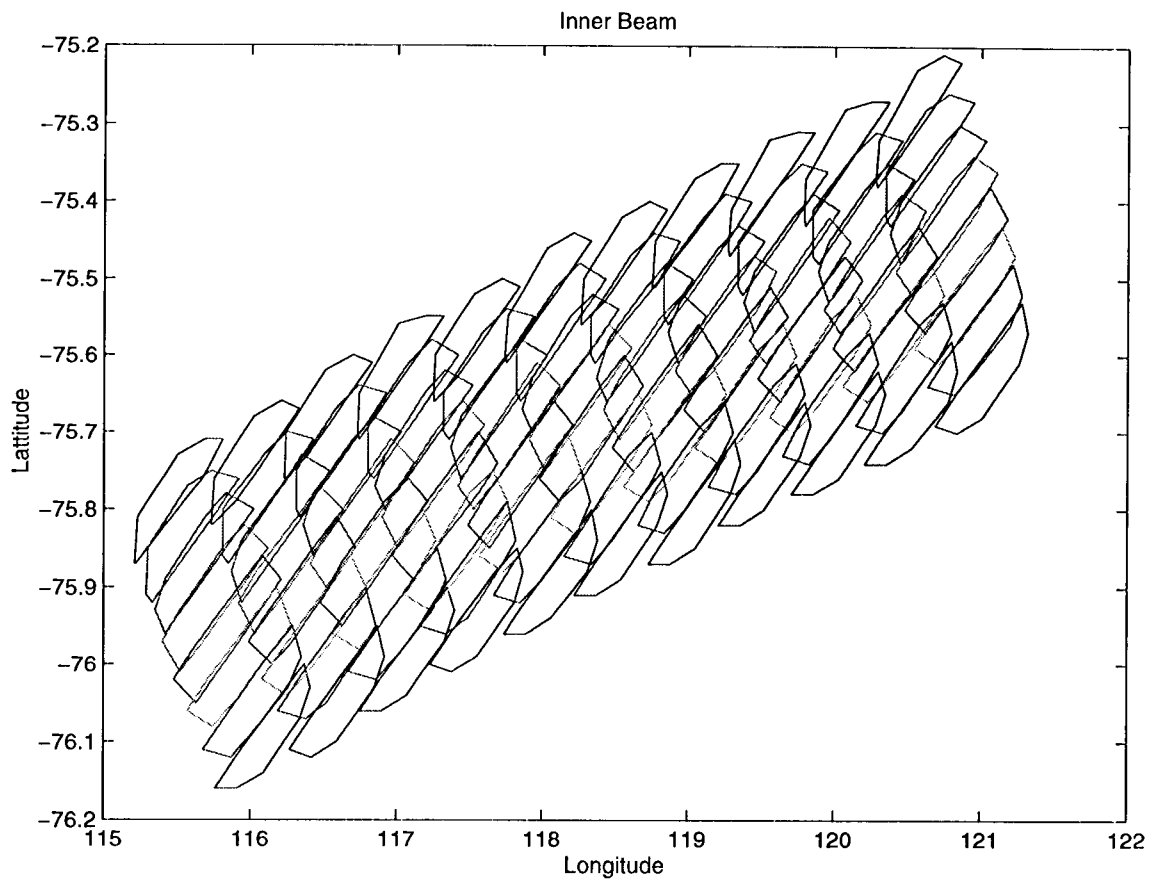


Figure 11: Center eight slice outlines for eleven consecutive transmit pulses for the inner antenna beam. Slice are outlines are given by approximations to the 3 dB spatial response contour.

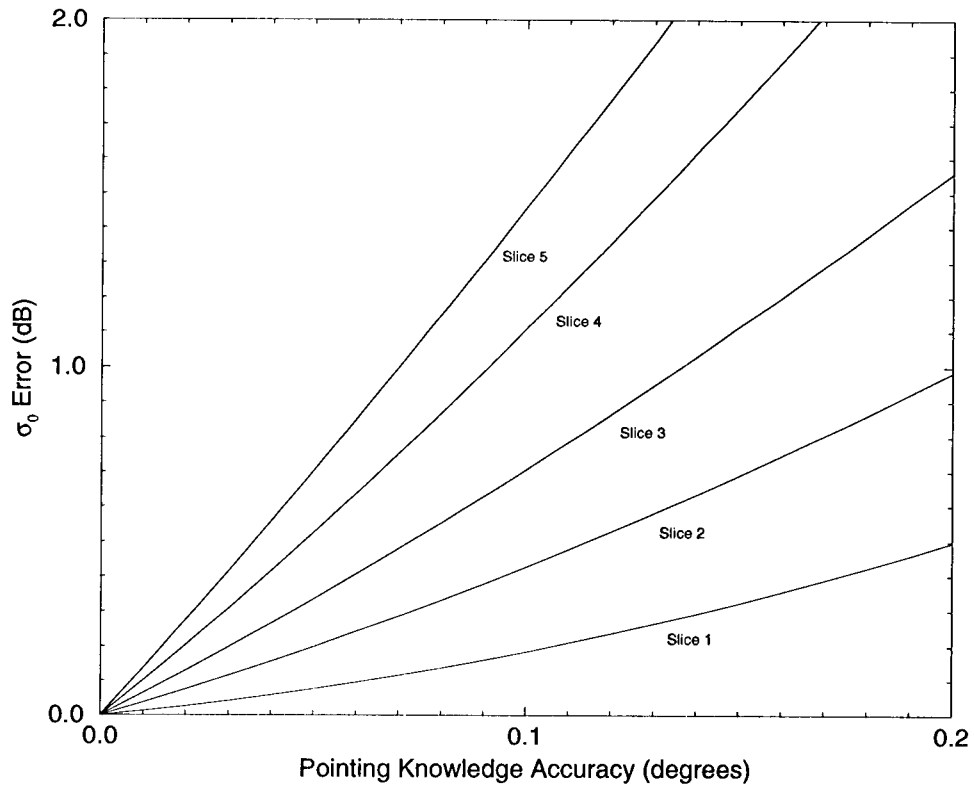


Figure 12: σ^o calibration (or, equivalently, X) error as a function of antenna pointing elevation angle knowledge accuracy. “Slice 1” is the inner-most slice (closest to antenna beam center), and “Slice 5” is the outer-most (on edge of antenna pattern).

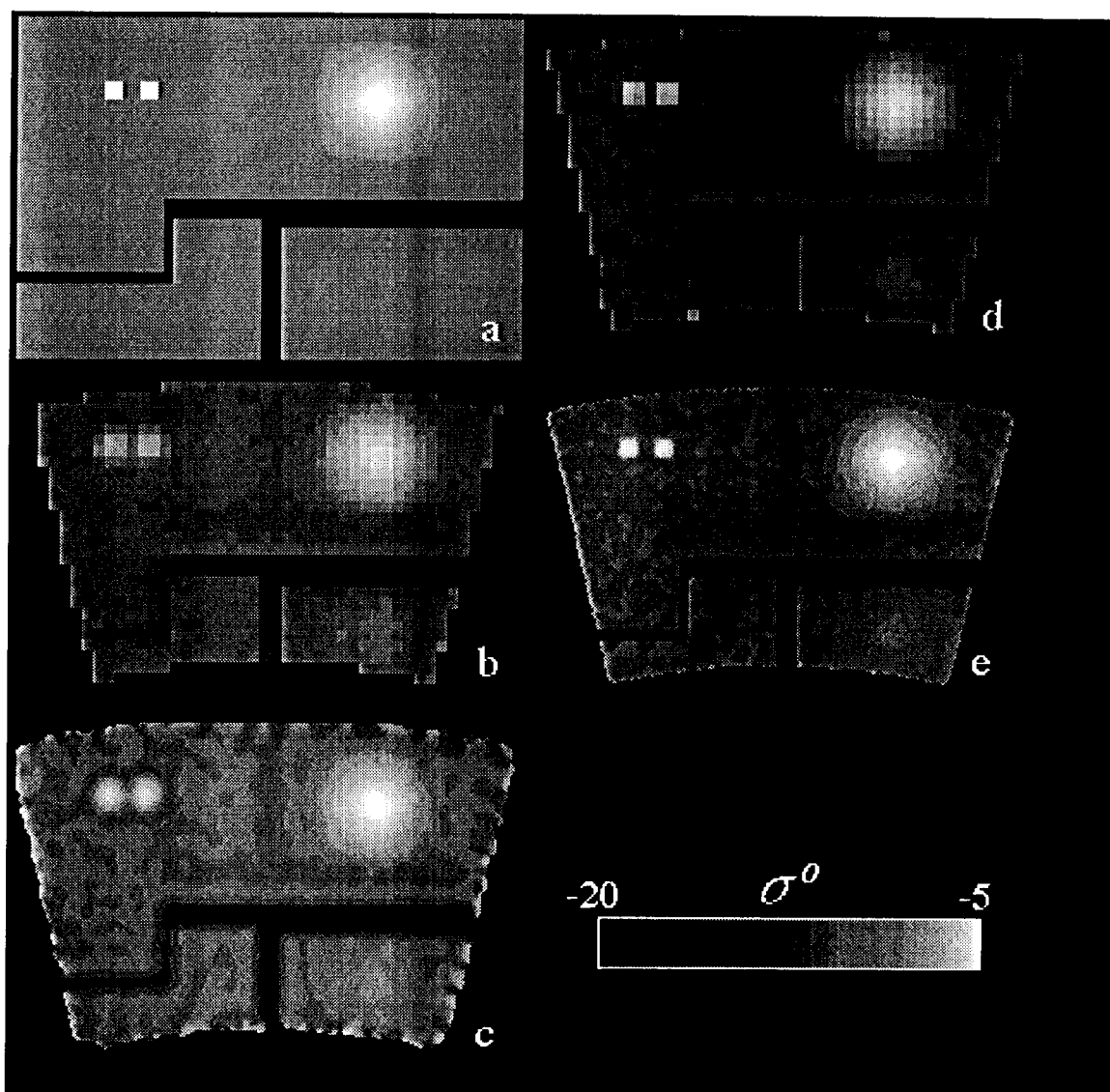


Figure 13: Simulated images from Quikscat/Seawinds. a) Simulated truth image. b) Gridded image (25 km grid) using beam-limited footprint [no slicing]. c) SIR-enhanced resolution image using beam-limited footprint. d) Gridded image using the 10 inner slices (25 km grid). e) SIRF-enhanced resolution image using slices. Pixel resolution is 4.5 km. The area is a small, synthetic region in Wilkes Land in Antarctica (hence the odd shape which is a box in lat/lon space but is mapped using a Lambert projection to a flat map).